



**UNIVERSITY OF LEEDS**

This is a repository copy of *High-throughput electrochemical sensing platform for screening nanomaterial-biomembrane interactions*.

White Rose Research Online URL for this paper:  
<http://eprints.whiterose.ac.uk/156376/>

Version: Accepted Version

---

**Article:**

Owen, J [orcid.org/0000-0003-0778-0858](https://orcid.org/0000-0003-0778-0858), Kuznecovs, M, Bhamji, R et al. (7 more authors) (2020) High-throughput electrochemical sensing platform for screening nanomaterial-biomembrane interactions. *Review of Scientific Instruments*, 91 (2). 025002. ISSN 0034-6748

<https://doi.org/10.1063/1.5131562>

---

Published under license by AIP Publishing. This is an author produced version of a paper accepted for publication in *Review of Scientific Instruments*. Uploaded in accordance with the publisher's self-archiving policy.

**Reuse**

Items deposited in White Rose Research Online are protected by copyright, with all rights reserved unless indicated otherwise. They may be downloaded and/or printed for private study, or other acts as permitted by national copyright laws. The publisher or other rights holders may allow further reproduction and re-use of the full text version. This is indicated by the licence information on the White Rose Research Online record for the item.

**Takedown**

If you consider content in White Rose Research Online to be in breach of UK law, please notify us by emailing [eprints@whiterose.ac.uk](mailto:eprints@whiterose.ac.uk) including the URL of the record and the reason for the withdrawal request.



[eprints@whiterose.ac.uk](mailto:eprints@whiterose.ac.uk)  
<https://eprints.whiterose.ac.uk/>

# High-throughput electrochemical sensing platform for screening nanomaterial-biomembrane interactions

Joshua Owen<sup>a,\*</sup>, Maksims Kuznecovs<sup>a</sup>, Raeesa Bhamji<sup>b</sup>, Nicola William<sup>b</sup>, Natalia Domenech-Garcia<sup>b</sup>, Michelle Hesler<sup>c</sup>, Thorsten Knoll<sup>c</sup>, Yvonne Kohl<sup>c</sup>, Andrew Nelson<sup>b</sup> and Nikil Kapur<sup>a</sup>

<sup>a</sup> *Institute of Thermofluids, School of Mechanical Engineering, University of Leeds, Leeds, LS2 9JT, United Kingdom*

<sup>b</sup> *School of Chemistry, University of Leeds, Leeds, LS2 9JT, United Kingdom*

<sup>c</sup> *Fraunhofer Institute for Biomedical Engineering IBMT, Joseph-von-Fraunhofer-Weg 1, 66280 Sulzbach, Germany*

## Abstract

A high-throughput, automated screening platform has been developed for the assessment of biological membrane damage caused by nanomaterials. Membrane damage is detected using the technique of analysing capacitance-current peak changes obtained through rapid cyclic voltammetry (RCV) measurements of a phospholipid self-assembled monolayer, formed on a mercury film deposited onto a microfabricated platinum electrode, after the interaction of a biomembrane-active species. To significantly improve wider usability of the screening technique, a compact, high-throughput screening platform was designed, integrating the monolayer-supporting microfabricated electrode into a microfluidic flow cell, with bespoke pumps used for precise, automated control of fluid flow. Chlorpromazine, a tricyclic antidepressant, and citrate-coated 50 nm diameter gold nanomaterial (AuNM) were screened to successfully demonstrate the platform's viability for high-throughput screening. Chlorpromazine and AuNM showed interactions with a 1,2-dioleoyl-sn-glycero-3-phosphocholine (DOPC) monolayer at concentrations in excess of 1  $\mu\text{mol dm}^{-3}$ . Biological validity of the electrochemically-measured interaction of chlorpromazine with DOPC monolayers was confirmed through quantitative comparisons with HepG2 and A549 cytotoxicity assays. The platform also demonstrated desirable performance for high-throughput screening, with membrane interactions detected in <6 min per assay. Automation contributed to this significantly, by reducing

---

\* Corresponding author: Joshua Owen (Email: J.J.Owen@leeds.ac.uk)

the required operating skill level when using the technique and minimising fluid consumption.

## **Keywords**

Phospholipid monolayer, gold nanomaterial, biomembrane interaction, microfluidic flow cell, mercury electrode, rapid cyclic voltammetry, high-throughput screening

## **1. Introduction**

Advances in nanotechnology have resulted in widespread usage of nanomaterials, often with applications in consumer products, biomedical and sensing technologies [1-4]. However, toxicity hazards associated with nanomaterials have been widely reported, with growing research in the field of nanotoxicology emphasising the need for screening techniques to characterise nanomaterial hazards [5-12]. As the applications for engineered nanomaterials continues to grow, high-throughput, *in vitro* screening solutions are essential to accelerate the process of evaluating the toxicity of novel engineered nanomaterials and to meet the demand for hazard identification [13, 14]. High-throughput *in vitro* toxicity sensing technologies also provide an alternative to *in vivo* animal toxicity studies, which have ethical implications and are not economically feasible for screening a vast range of nanomaterials [3, 15, 16].

Understanding cytotoxicity remains a particularly important and significant challenge in the field of nanotoxicology, as nanomaterials, due to their small size, can have unique properties that influence the mechanisms of interaction with cell membranes [17]. Engineered nanomaterials can interact with cell membranes through adsorption onto the membrane, penetration through the membrane and endocytosis [17-21]. The understanding of nanomaterial cytotoxicity is challenging due to the complexity of cell membranes and the wide range of nanomaterial parameters, such as particle size, material and shape, that can influence the mechanisms of membrane interaction [5, 7, 10, 11, 17, 21]. Cell-based *in vitro* toxicity assays are typically employed for the assessment of nanomaterial cytotoxicity, which are adapted for high-throughput screening through the use of high quantity multi-well plate platforms [22-24]. However, generally there

remains a lack of high-throughput techniques for *in vitro* assessment of nanomaterial hazards.

One solution to rapid screening of the interaction of nanomaterial with biological membranes is the application of a membrane-on-chip sensing technique, one of which measures an electrochemical response to detect interaction with a phospholipid, self-assembled monolayer supported on a mercury (Hg) electrode [25-35]. This has been well-established as an effective technique for quantifying and mechanistically understanding biomembrane interaction. The interaction with the monolayer is evaluated through highly sensitive and rapidly detectable changes in capacitance-current peaks after the interaction of a biomembrane-active compound or particle with the Hg-supported monolayer, measured through the application of rapid cyclic voltammetry (RCV). A strong correlation exists between biomembrane interaction measured using the monolayer technique and physical membrane damage of a more complex biological bilayer membrane, confirmed through direct comparison with phospholipid unilamellar vesicle studies [21, 36].

Recently, the technique has been improved through the use of a microfabricated electrode, consisting of platinum (Pt) discs on to which Hg can be deposited to support the phospholipid monolayer [25, 26], as opposed to a hanging Hg drop electrode used in original studies by Nelson [28], enabling safe and robust use of Hg as a working electrode in a flow environment. Another significant advantage of this is that the phospholipid monolayer can be rapidly re-established after measurement to create a reusable electrode, ideal for high-throughput screening. This is advantageous compared to other high-throughput *in vitro* methods, such as high quantity, multi-well plate cell-based assays, which require a longer time period to obtain meaningful results [14, 23]. This also reduces the possibility of nanomaterial transformations (e.g. aggregation) during assessment, which have been reported to contribute to ambiguity in cell assay studies [37-39]. However, despite robust characterisation and validation of the sensing technique [40], limitations still exist, such as a complex operating procedure and excessive fluid consumption, preventing its wider adoption for high-throughput hazard assessment of nanomaterials.

With advances in microfluidic flow cell technology and the possibility to automate processes, significant potential exists to improve the current screening methodology, as most recently described by Vakurov et al. [7], to reduce fluid consumption, increase throughput and improve usability. Microfluidic flow cells offer significant benefits for high-throughput biosensing applications, by reducing fluid consumption in a low cost and easy to manufacture, high precision cell [41-47]. The application of microfluidic technology is particularly advantageous for nanomaterial toxicity screening, enabling consistent transport of nanomaterial in high precision laminar fluid flow and being well-suited for automation [16]. Automation of the sensing technique also offers the potential to reduce required operator skill level by simplifying the screening process.

This study details the development of a new automated screening platform, incorporating a microfluidic flow cell, containing an Hg-supported membrane monolayer, for high-throughput sensing of nanomaterial-biomembrane interactions. The new screening platform offers a significant enhancement on the previous generations of the biomembrane-sensing system to create a rapid, high-throughput sensor viable for *in vitro* screening of nanomaterial-membrane interaction, decreasing required operator skill levels and decreasing fluid consumption. Gold nanomaterial (AuNM) and chlorpromazine, a pharmaceutical compound, were screened using the screening platform to demonstrate its viability as a high-throughput sensor for assessing biomembrane interactions of nanomaterial and to prove equivalence to well-validated studies using the sensing technique.

## **2. Automated Screening Platform Design**

### **2.1. Overview of Screening Technique**

A schematic of the sensing technique is provided in Figure 1 to demonstrate how biomembrane activity is assessed through RCV analysis. After supporting the phospholipid monolayer onto a Hg electrode, the characteristic RCV response consists of two capacitance-current peaks on the forward and reverse scans when the phospholipid 1,2-dioleoyl-sn-glycero-3-phosphocholine (DOPC) is used [40]. A biomembrane-active species (e.g. nanoparticles) can adsorb to and/or penetrate the monolayer, during flow across the coated electrode, suppressing the capacitance-current and/or shifting the

potential of peaks measured using RCV. The first capacitance-current peak on the forward scan, labelled 'A' in Figure 1, is often of significant interest to the operator and this peak is used to provide a quantitative indication of a species interaction with the monolayer. The capacitance current peak represents a monolayer phase change corresponding to ingress of electrolyte into the phospholipid monolayer [28, 40].

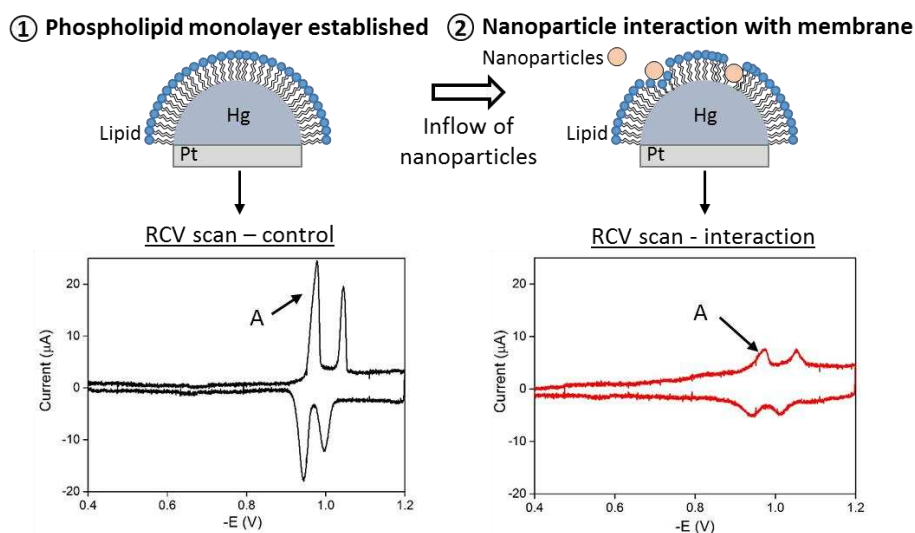


**Figure 1: Schematic of the screening technique to evaluate biomembrane interaction of nanomaterial with an Hg-supported phospholipid membrane monolayer through analysis of a RCV response, with peak 'A' highlighting the capacitance-current peak used to provide a quantitative comparison of biomembrane interaction**

The aim of the automated platform design was to utilise this well-established sensing technique and create an easy-to-use, high-throughput, *in vitro* sensing platform for rapid screening of nanomaterials. A critical analysis of the previous state of the technology (the methodology as described by Vakurov et al. [7]) was completed to identify limitations of the method, leading to the following objectives being set as criteria for the screening platform design. These objectives will enable wider potential use of the technique for assessment of nanomaterial hazards:

- i. The screening process was to be automated, thus significantly decreasing the complexity of the screening procedure and improving repeatability of the system to enable an inexperienced operator to use the screening system reliably and with minimal guidance.
- ii. The time required to screen nanomaterials was to be reduced, thus improving throughput and enhancing the feasibility of the technique for screening vast quantities of nanomaterials.

- iii. The screening platform was to be compactly designed, avoiding the use of large and numerous components to reduce space requirements and enable the device to be portable, improving feasibility of the design as a single screening platform.
- iv. A graphical user interface was to be developed to simplify control of the system, making the system easy-to-use for inexperienced operators, requiring minimal control to complete the screening process and therefore contributing to improved throughput.
- v. Fluid consumption and waste was to be reduced by optimising flow rates and volumes consumed through automation and reducing tubing usage to make the technique more viable for screening vast quantities of nanomaterial.

The newly-developed automated screening platform is shown in Figure 2, consisting of a microfluidic flow cell containing the phospholipid monolayer supported on a Hg sensing electrode, four automated bespoke syringe pumps enabling storage and transportation of fluids (electrolyte, test sample, phospholipid and water) into the flow cell, a field-programmable gate array (FPGA) data acquisition and control unit used to interface between software and hardware and an ACM Research Potentiostat for electrochemical measurements. A laptop was connected to control the screening platform, interfacing with syringe pumps and the FPGA control unit. The components of the platform are discussed in more detail in the following sections.

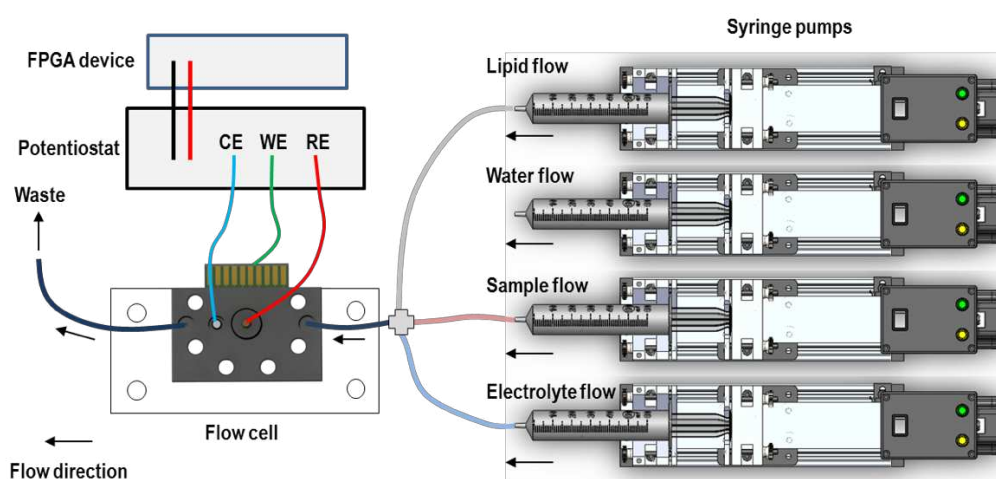


**Figure 2: Automated platform used for electrochemical analysis of biomembrane activity of compounds and particles after interaction with an Hg-supported phospholipid monolayer, consisting of a microfluidic flow cell, four syringe pumps, an FPGA data acquisition and control unit and a potentiostat, where RE is the reference electrode, CE is the counter electrode and WE is the working electrode**

## 2.2. Microfluidic Flow Cell and Sensing Electrode

A microfluidic flow cell was designed to transport fluids consumed in the screening process to the sensing electrode, contained within the flow cell, for electrochemical analysis. A layered approach was used for the microfluidic flow cell design, with flow cell layers fabricated using a laser cutter. This allows an inherently 3D structure to be established with the ability to seal ancillary components into the flow cell. Cast poly(methyl methacrylate) (PMMA) was employed for harder layers of the flow cell and Pt-cured silicone sheet was used for softer layers. The flow cell components were fastened together using bolts to provide a compression seal between softer and harder layers to prevent leakage of fluids and enable electrochemical measurements, by isolating electrical connections from contact with electrolyte. The design is both robust and provides excellent sealing.

The microfluidic flow cell is shown in Figure 3. The main components of the design include (1) a ceramic junction screw-type silver/silver chloride (Ag/AgCl) reference electrode containing 3 M NaCl gel (ALS); (2, 5 and 8) PMMA layers; (3) a 25 mm long Pt rod with 3.0 mm diameter (Goodfellow), used as the counter electrode, mounted in the flow cell downstream of the working electrode using a flangeless nut and ferrule; (4, 6 and 8) silicone layers to channel fluids through the flow cell and/or seal the flow cell and (7) a microfabricated Pt/Hg sensing electrode (supplied by Tyndall National Institute, Ireland). The Pt/Hg electrode consisted of eight Pt discs (12), with radii of 0.48 mm (of which two discs were deposited with Hg prior to insertion in the flow cell). Silicon nitride-insulated electrical contacts enabled potentiostat connection to the Pt/Hg electrode (13).

Fluids were transported into and out of the flow cell with a 1/16" inner diameter, 1/8" outer diameter, fluorinated ethylene propylene (FEP) tubing, mounted in the inlet and outlet ports on the flow cell (layer 2) through the use of standard fittings (1/4-28 Unified National Fine (UNF) flangeless threaded nuts). FEP tubing was used for chemical resistance and compatibility with test compounds and particles to prevent contamination. Fluids were transported out of the flow cell and into a waste container. Syringes containing test fluids were connected to tubing via a two-way shut off valve, closed to prevent air bubbles from entering the system when replacing syringes. The tubing from each syringe was connected to a polyether ether ketone cross component, to mix fluids prior to the flow cell inlet.

Nanomaterial transport through microfluidic flow cells provides an additional design challenge, with some microfluidic devices reported to have been ineffective at transporting nanomaterials to sensing areas and cell assay well plates [47]. Challenges with microfluidic design for nanomaterial transport include ensuring no aggregation, minimising entrapment, preventing air bubbles and decreasing sedimentation of nanomaterial in fluid tubing [16]. Aggregation and sedimentation of nanomaterial was minimised by using short tubing lengths. Nanomaterial was mixed with electrolyte flow just prior to the flow cell inlet, rather than further upstream, to minimise the possibility of aggregation. Measurements were completed in continuous flow, also decreasing potential time for aggregation of nanomaterial. Entrapment of nanomaterial was not observed as a result of minimising the number of components in the fluid flow path. Whilst appearing mechanically complex, from a flow perspective the flow channel within the flow cell is simple. Critically the dead spaces around ancillary components (e.g. the reference and counter electrodes and piping connections) were minimal reducing the chance of entrapment of nanomaterial and therefore reducing demand in cleaning between subsequent measurements. Nanomaterial was easily flushed through and removed from the system during cleaning, confirmed by the RCV response.

To confirm the flow cell effectively transported species to the sensing electrode, as highlighted in Figure 3, and to confirm no undesirable flow conditions (such as flow recirculation as the flow channel width expands [48, 49]) influenced transport to the sensing electrode, computational fluid dynamics (CFD) simulations using COMSOL Multiphysics 5.3a [50] were completed to predict species transport through the flow channel after solving a finite element discretisation of the Navier-Stokes equations for laminar fluid. Full details of the methodology used to complete these simulations are provided in the Supplementary Material.

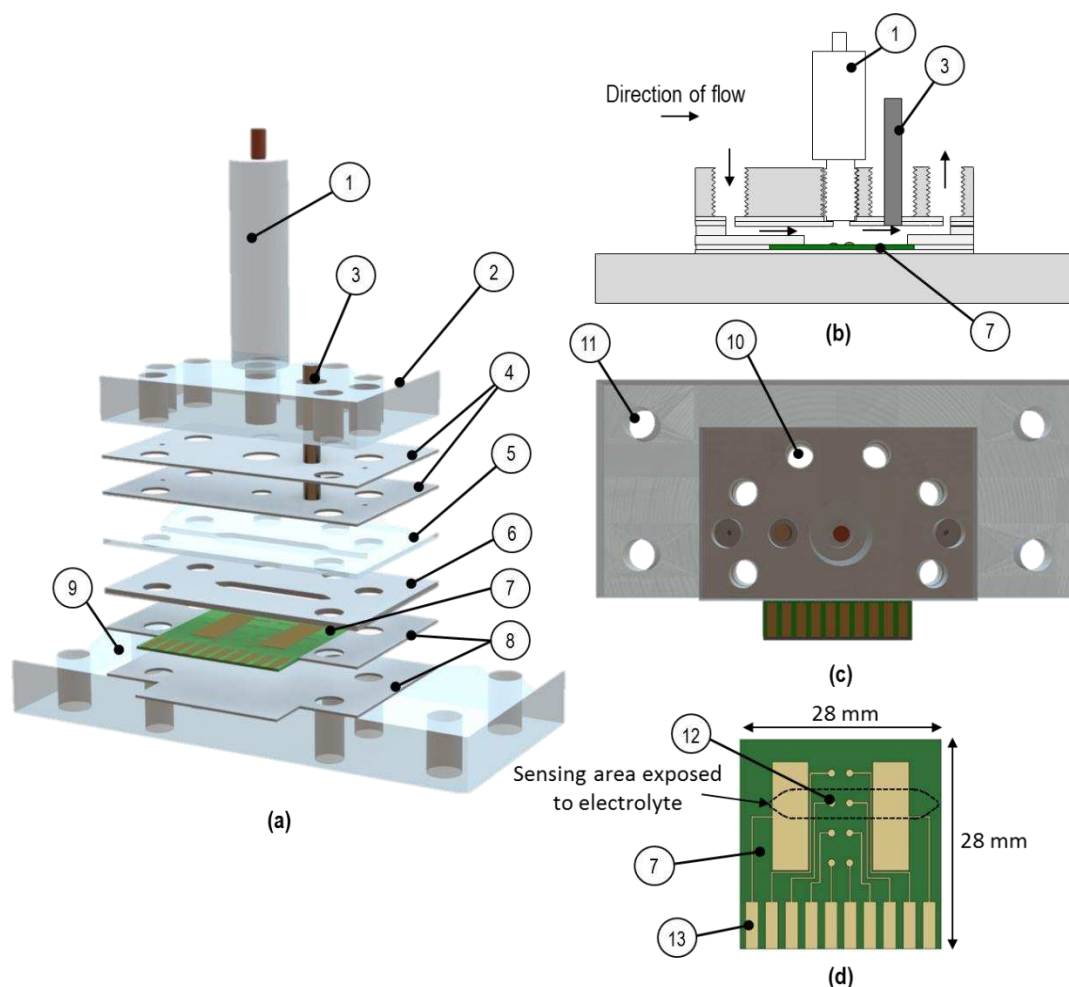


**Figure 3: Microfluidic flow cell showing (a) exploded assembly of components, (b) cross-section schematic of the flow cell, (c) top view of the flow cell assembly and (d) microfabricated sensing Pt/Hg electrode, consisting of (1) Ag/AgCl reference electrode, (2) PMMA top plate, (3) Pt rod counter electrode, (4) silicone fluid inlet/outlet layers, (5) PMMA flow channel layer, (6) silicone sensing layer, (7) microfabricated sensing Pt/Hg electrode, (8) silicone layers for electrode support and sealing, (9) PMMA bottom layer, (10) screw holes x 6 to mount and seal flow cell, (11) screw holes x 4 to mount sealed flow cell on aluminium breadboard, (12) Pt working electrode and (13) electrical contacts, sealed from the electrolyte, for potentiostat connection**

### 2.3. User Control Interface

An easy-to-use graphical user interface, shown in the Supplementary Material, was developed in LabVIEW to enable operator control of the screening platform and to display relevant information to the operator. The user interface consisted of operator controls to specify the size of the syringe used and the volume of fluid contained in the syringe for electrolyte, lipid, screening test sample and water; operator controls to specify the fluid flow rates and potentials for RCV measurements and the RCV response

from which data could be easily extracted. An FPGA data acquisition and control unit controlled the potentials applied by the potentiostat, as determined by the operator on the user interface, and acquired the resulting electrochemical data, presented on the user interface. This enabled the operator to screen nanomaterials with minimal effort, switching between the different processes of the screening procedure with ease, significantly reducing the time required to complete a screening programme.

### 3. Experimental

#### 3.1. Materials

AuNM and chlorpromazine were screened to assess interaction with the Hg-supported phospholipid monolayer. The phospholipid used was DOPC, a common component of biological membranes, purchased as 99% pure (Avanti Polar Lipids Alabaster, AL). A minimum dispersion of  $0.5 \text{ mmol dm}^{-3}$  of DOPC with Milli-Q water ( $18.2 \text{ M}\Omega$ ) was prepared and mixed by gently shaking. The control electrolyte was  $0.1 \text{ mol dm}^{-3}$  KCl (calcined at  $600^\circ\text{C}$  for 2 h) and buffered at pH 7.4 with  $0.01 \text{ mol dm}^{-3}$  phosphate (phosphate buffered saline or PBS, referred to as 'Buffer' on the screening platform control interface).

Chlorpromazine (Sigma-Aldrich), a tricyclic antidepressant with the compound molecular structure shown in the Supplementary Material, has been regularly screened and shown to be highly biomembrane-active in previous studies using the RCV phospholipid monolayer membrane-on-chip technique [25, 26]. Therefore, interactions of chlorpromazine with the monolayer were assessed to confirm the validity of results measured using the new platform at concentrations ranging from  $10^{-5}$  to  $10^4 \text{ }\mu\text{mol dm}^{-3}$ . Chlorpromazine was also used for comparison with cytotoxicity assays to confirm biological relevance of the electrochemically-measured membrane interactions through cell viability studies.

Dispersions of citrate-coated AuNM (Alfa Aesar) with a diameter of 50 nm were screened in a concentration range from  $10^{-3}$  to  $10^2 \text{ }\mu\text{mol dm}^{-3}$  to evaluate the RCV response after interaction with the Hg-supported DOPC monolayer and to demonstrate the performance of the platform as a viable solution to high-throughput *in vitro* screening of nanomaterials. AuNMs have been shown, in some cases, to be cytotoxic, potentially as a

result of cell membrane penetration [11, 51], so were chosen to be investigated in this study to demonstrate interaction with a DOPC membrane. The dispersion of AuNM was reported as a concentration of  $\mu\text{mol dm}^{-3}$  of Au in the dispersion, confirmed by inductively coupled plasma mass spectrometry (PerkinElmer SCIEX ELAN DRC-e with a PerkinElmer S10 auto sampler) after digestion of known volumes of AuNM, from the citrate-coated AuNM stock dispersion, in aqua regia. By determining elemental concentration of Au using this technique, the appropriate volume of AuNM was dispersed in Milli-Q water to achieve the Au concentrations reported.

The size of the AuNM was confirmed using dynamic light scattering (DLS) measurements on a Malvern Instruments nanoZS Zetasizer prior to the test by dispersing the AuNM in a Milli-Q water medium, showing an average particle diameter of 68 nm, based on intensity plots vs particle diameter in Figure 4. To confirm that aggregation of the AuNM would not be significant after the dispersion mixed with PBS during flow through the flow cell, AuNM was dispersed in PBS and DLS measurements were completed after 5 min and 20 min of incubation, with all AuNM expected to flow through the flow cell within 1 min of mixing with PBS during screening tests. No aggregation was measured during that period, as shown in Figure 4 by equivalent size distribution observed between the AuNM samples. A scanning electron microscope (SEM) was used to image the AuNM, showing the approximate size and shape of the AuNM used in the study in Figure 4. Images were obtained by drying an AuNM dispersion on an SEM stub and using an FEI Nova NanoSEM 450 at an operating voltage of 5 kV in the concentric back scattering mode.

To prepare the microfabricated electrode, prior to insertion in the flow cell, it was cleaned in Piranha solution for approximately 15 min, rinsed with Milli-Q water and dried. After cleaning, Hg was deposited onto two Pt bases prior to mounting in the flow cell. Once contained within the flow cell, an RCV potential excursion from  $-0.4\text{ V}$  to  $-3.0\text{ V}$  at a scan rate of  $100\text{ V s}^{-1}$  was completed, for approximately 30 min, maintained under PBS throughout this period in static conditions to ensure robust adhesion of the Hg to the Pt substrate was achieved and any organic material from the Hg surface was removed. A more detailed method for preparation of the microfabricated Pt/Hg electrode is provided by Rashid et al. [32].

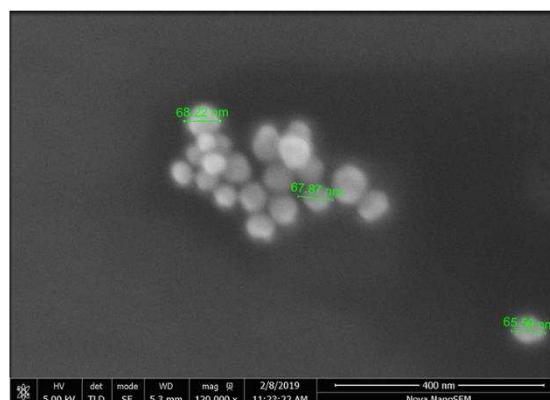
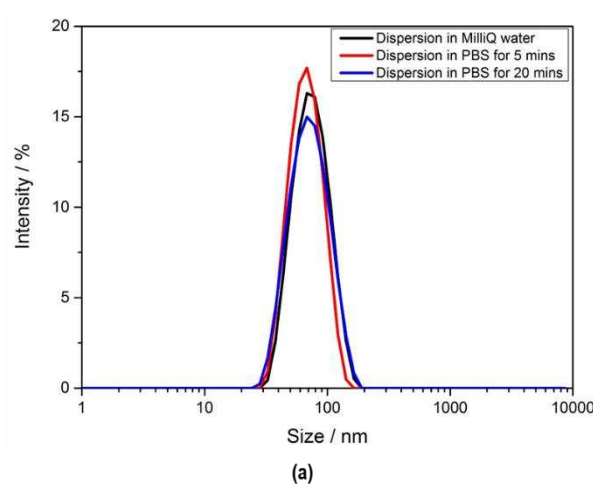


**Figure 4: (a) Intensity plot from DLS measurements of particle size distribution for AuNM dispersions in Milli-Q water and PBS, showing average particle diameter of 68 nm and no aggregation within 20 minutes in PBS (where time in min is the time at the end of completed measurements), (b) an SEM image of the size distribution of AuNM and (c) a higher magnification SEM image showing the approximate size of AuNM used in the study**

### 3.2. Screening Methodology – Automated Platform

The fluids used during the screening procedure (PBS, DOPC and sample) were prepared prior to testing by bubbling with argon gas, for a minimum period of 30 min prior to screening, to exclude dissolved oxygen ( $O_2$ ) in the fluids. After excluding  $O_2$ , individual syringes were filled, mounted on the platform and connected to the tubing. RCV scans were completed by applying potential excursions between two potentials at a specified scan rate, depending on the stage of the screening procedure. The four stages, controlled from the user interface as shown in the Supplementary Material, consisted of an ‘Idle’, ‘Clean’, ‘Lipid’ and ‘Sample’ stage.

### ***3.2.1. Idle Response***

During the 'Idle' stage a potential excursion from  $-0.4\text{ V}$  to  $-1.2\text{ V}$  was completed at a scan rate of  $40\text{ V s}^{-1}$  in static conditions, so the RCV response could be analysed after each stage of the process. No fluid was flushed into the flow cell during this stage to allow for analysis of the RCV response. An appropriate control RCV response, prior to sample injection, could be confirmed by the operator and the resulting change in the RCV response after the sample was injected could be analysed. Data was exported from the 'Idle' stage, where RCV responses were exported for further analysis.

### ***3.2.2. Flow Cell Clean***

During the 'Clean' stage, a potential excursion of  $-0.4\text{ V}$  to  $-3.0\text{ V}$  was completed at a scan rate of  $100\text{ V s}^{-1}$  under PBS flow at a constant flow rate of  $4.0\text{ cm}^3\text{ min}^{-1}$  to flush any remaining sample (and other contaminants) out of the flow cell into a waste container. A minimum of  $5\text{ cm}^3$  of buffer was used to clean the flow cell after each measurement.

### ***3.2.3. Supporting a Phospholipid Membrane Monolayer on Hg***

Once cleaned, DOPC was flushed into the flow cell at a flow rate of  $1.0\text{ cm}^3\text{ min}^{-1}$  in the 'Lipid' stage. A potential excursion of  $-0.4\text{ V}$  to  $-3.0\text{ V}$  was completed at a scan rate of  $100\text{ V s}^{-1}$  under PBS flow at a constant flow rate of  $4.0\text{ cm}^3\text{ min}^{-1}$ , before returning to the 'Idle' stage to assess the RCV response. A total of  $0.5\text{ cm}^3$  of DOPC was injected to create a stable monolayer on the Hg electrode, confirmed through analysis of the RCV response showing the characteristic peaks, specific to the phospholipid in use, at appropriate potentials [25].

### ***3.2.4. Sample Interaction with Phospholipid Membrane Monolayer***

To assess interaction with the DOPC layer, a test sample was flushed in during the 'Sample' stage at a flow rate of  $1.0\text{ cm}^3\text{ min}^{-1}$  with PBS at a flow rate of  $4.0\text{ cm}^3\text{ min}^{-1}$ . A potential excursion from  $-0.4\text{ V}$  to  $-1.2\text{ V}$  was completed at a scan rate of  $40\text{ V s}^{-1}$ , similarly to the 'Idle' stage, to observe how the peaks changed in real-time during flow of sample through the flow cell. All sample concentrations were screened three times by

evaluating samples in order of increasing concentration, starting with the lowest concentration. Another three repeats were completed by screening samples in a random order, to ensure that results were not influenced by the order in which sample concentrations were screened.

After completing a measurement, the syringe containing the test sample was cleaned with MilliQ water (or replaced if a significant interaction was observed). A total of 2 cm<sup>3</sup> of PBS was also injected through the tubing connected to the sample syringe to flush any remaining sample through the tubing and into the waste container. The PBS, DOPC and sample syringes were replaced after all sample concentrations were screened, prior to completing repeat measurements. The flow cell was then cleaned by selecting the 'Clean' process on the user interface to remove any remaining DOPC on the Pt/Hg electrode and flush out sample, re-establishing the Pt/Hg electrode as a clean sensor available for the next measurement.

### **3.3. Screening Methodology – Predecessor System**

A comparison was made with the well-validated predecessor membrane-on-chip sensor, by screening the same samples on both systems. A detailed description of the system and methodology for its use is provided by Vakurov et al. [7]. Sample preparation was completed using the same methodology and the screening process was completed in the same order as for the automated platform using an identical electrochemical procedure. PBS was stored in a 0.5 dm<sup>3</sup> reservoir on the manual system and transported to the flow cell using a peristaltic pump to maintain a flow rate of 4.67 cm<sup>3</sup> min<sup>-1</sup>. The total volume flow of PBS used to screen the compounds could not be precisely controlled. DOPC and samples were injected into the PBS flow manually using a syringe, upstream of the flow cell. For this reason, flow rates of DOPC and sample were not controlled and volumes of fluid flushed through the cell were not precisely known or consistent for all measurements. For electrochemical measurements a Ag/AgCl 3.5 mol dm<sup>-3</sup> KCl reference electrode was fitted into the flow cell. The counter electrode on the microfabricated electrode was used, with a much greater electrode area exposed in the manual system flow cell, due to a different flow cell design. An Autolab PGSTAT12 potentiostat was used for electrochemical measurements.

### 3.4. Cytotoxicity Assays

To confirm equivalence between the automated RCV platform and well-established *in vitro* techniques, cell viability assays were performed with two widely used cell lines: HepG2 (human hepatocellular carcinoma cells) and A549 (alveolar epithelial cells), both purchased from Leibniz-Institut DSMZ-Deutsche Sammlung von Mikroorganismen und Zellkulturen GmbH (cell line no. ACC-180 and ACC-107, Braunschweig, Germany). Both cell lines were cultured in Roswell Park Memorial Institute medium (RPMI1640, R8758, Sigma-Aldrich, Germany) supplemented with 10% v/v fetal bovine serum (FBS, 26140-079 ThermoFisher Scientific, Germany), 100 U/ml penicillin and 100 µg/ml streptomycin (5070-63, ThermoFisher Scientific, Germany) in a humidified incubator at 37 °C with 5% CO<sub>2</sub> atmosphere. For the exposure with chlorpromazine, the cells were seeded at a density of 10,000 cells per well in a 96 well plate and cultured for 24 hours. The stock solution of chlorpromazine was freshly prepared for all experiments and diluted at the desired concentration in cell culture medium. Cell culture medium without chemical was used as negative control. The cells were exposed with chlorpromazine in doses ranging from 5 to 100 µmol dm<sup>-3</sup> for 24 hours. The cell viability reagent alamarBlue (Invitrogen, Germany) was diluted 1:10 in fresh culture medium and incubated with the cells for 1 h at 37 °C. The fluorescence (excitation 530 nm, emission 590 nm) was determined and the values were blank corrected. The viability of the control cells was set to 100%. Three independent experiments were performed with each cell line and at least three single wells per test condition.

## 4. Results and Discussion

### 4.1. Simulation of Species Transport in Flow Cell

The transport of chlorpromazine through the flow cell at a constant flow rate of 4.0 cm<sup>3</sup> min<sup>-1</sup> is shown in Figure 5, represented by the concentration ( $c$ ) along the bottom surface, relative to the inflow concentration ( $c_{in}$ ) to confirm appropriate transport of the species to the sensing electrode. The average concentration of chlorpromazine over the approximate surface area of the electrodes on the Pt/Hg electrode was determined from the predictions and shown in Figure 5. The error bars plotted in Figure 5 represent the maximum and minimum concentration predicted over the surface area of the electrode

at a particular time. A concentration at the electrode equal to the desired inflow concentration ( $c/c_{in} = 1.0$ ) was achieved within approximately 15 s of flow through the flow cell, showing the flow cell design was effective.

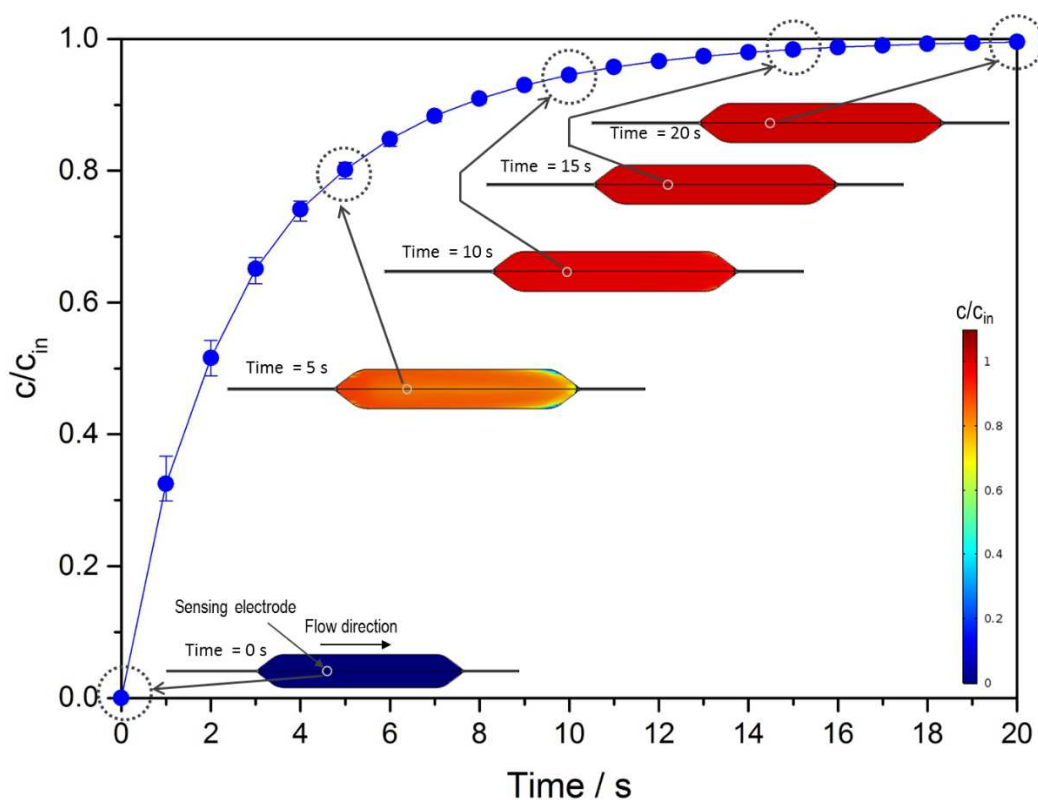


**Figure 5: CFD simulations of time-dependent transport through the flow cell, showing the concentration ( $c$ ) on the bottom of surface of the flow cell (i.e. the location of the electrode), relative to the inflow concentration ( $c_{in}$ ) of chlorpromazine under steady state flow through the flow cell at a flow rate of  $4.0 \text{ cm}^3 \text{ min}^{-1}$  and showing the average concentration over the surface area of the electrode positioned 17.6 mm from the flow inlet**

## 4.2. Chlorpromazine

The RCV scans for chlorpromazine interactions (red line) measured using the new automated platform are shown in Figure 6 and are compared against the DOPC baseline (black line) response. The scans for all concentrations are given in the Supplementary Material. No significant interaction between chlorpromazine and DOPC was observed at low concentrations, but at concentrations above  $1 \mu\text{mol dm}^{-3}$ , a significant interaction was measured. The interactions caused suppression of the capacitance-current peaks, measured between potentials of  $-0.95 \text{ V}$  and  $-1.05 \text{ V}$ , which, at high concentrations, were completely suppressed. Suppression of the capacitance-current peaks after an

interaction is typically caused by adsorption onto the DOPC monolayer, influencing the fluidity of the phospholipid layer [10].

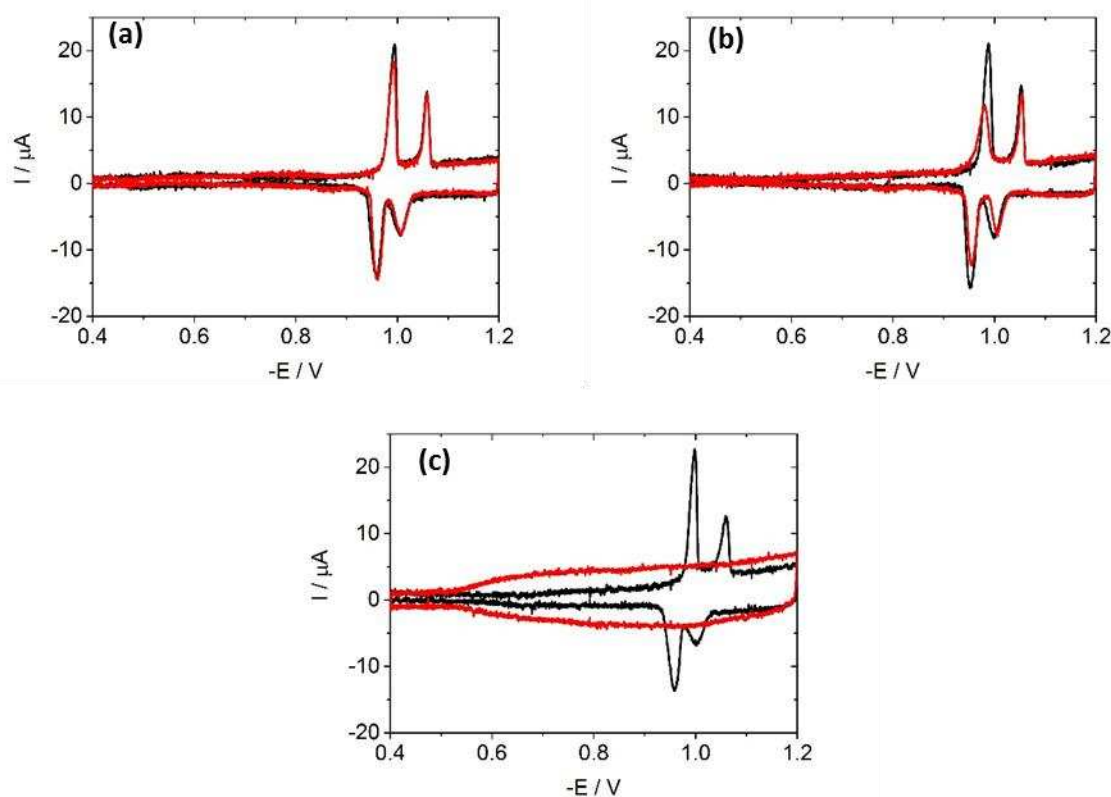


**Figure 6: RCV scans, measured using the automated screening platform at a scan rate of  $40 \text{ V s}^{-1}$ , of an Hg-supported DOPC monolayer (black line) and interaction with chlorpromazine (red line) in concentrations of (a)  $10^{-5} \text{ } \mu\text{mol dm}^{-3}$ , (b)  $10 \text{ } \mu\text{mol dm}^{-3}$  and (c)  $10^4 \text{ } \mu\text{mol dm}^{-3}$  in PBS at pH 7.4 (all RCV scans in the Supplementary Material)**

The influence of chlorpromazine concentration on the first measured capacitance-current peak height (the peak labelled as peak A in Figure 1 and shown on the forward scans in Figure 6 at potentials of  $-0.96 \text{ V}$ ) is shown in Figure 7, recorded as a suppression of the peak after interaction with chlorpromazine, relative to an average baseline peak height measured for a stable DOPC monolayer. The average height of the capacitance-current peak of the DOPC monolayer was  $19.5 \text{ } \mu\text{A}$  with a standard deviation of  $\pm 1.4 \text{ } \mu\text{A}$ , based on thirty measurements of the RCV response. The average percentage peak suppression is shown in Figure 7 from six measurements of chlorpromazine interaction for each concentration, with error bars representing the standard deviation. Results were compared by screening chlorpromazine using the well-validated manual system to demonstrate equivalence with the automated platform. The average height of the capacitance-current peaks of the DOPC monolayer obtained using the manual system was

20.9  $\mu\text{A} \pm 1.5 \mu\text{A}$ , similarly determined from an average of thirty measurements. An average of three measurements is shown for the chlorpromazine concentrations screened on the manual system, with error bars representing the standard deviation. More measurements were completed using the new automated platform to demonstrate repeatability, robustness and durability of the newly-designed platform. The average difference between peak suppression measured on the automated and manual system for all concentrations was 4%.

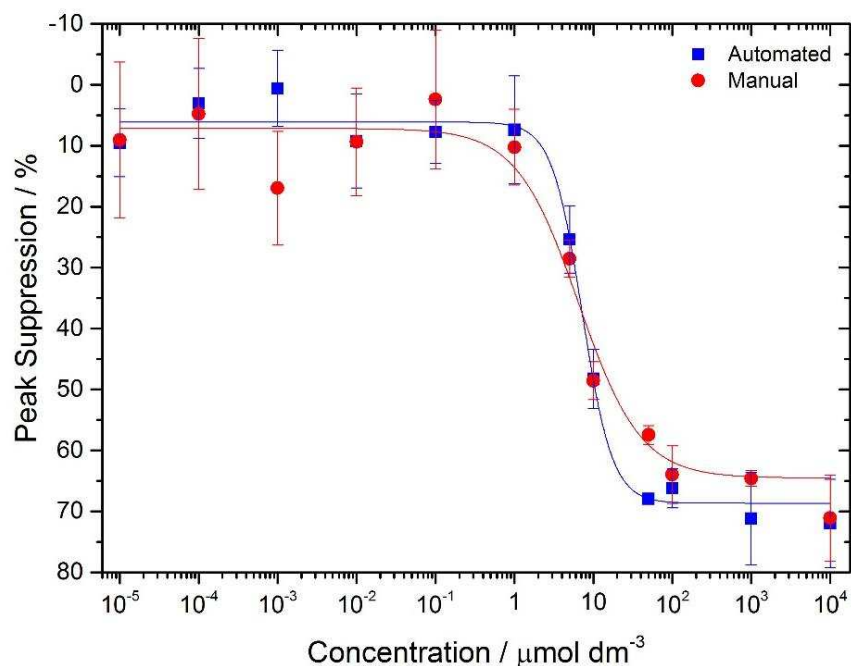


**Figure 7: Percentage suppression of first capacitance-current peak observed on the forward scan of RCV measurements, at a potential of approximately  $-0.96 \text{ V}$ , after interaction of chlorpromazine at different concentrations with an Hg-supported DOPC monolayer in PBS at pH 7.4, showing equivalence between the new automated platform and the manual predecessor biomembrane sensing system**

The automated platform dose response curve was compared with in vitro cell viability studies in HepG2 and A549 cells in Figure 8. The comparison was made over the range of concentrations from where the peak suppression became statistically significant to the maximum possible interaction ( $5 \mu\text{mol dm}^{-3}$  to  $100 \mu\text{mol dm}^{-3}$ ). RCV peak suppression was normalised against the average maximum peak suppression recorded at  $10,000 \mu\text{mol dm}^{-3}$  in Figure 7 (72%), to enable direct comparison with the cell viability studies (reported in a measurement range from 0 to 100%). Error bars for the cell viability studies show the standard deviation from three measurements.

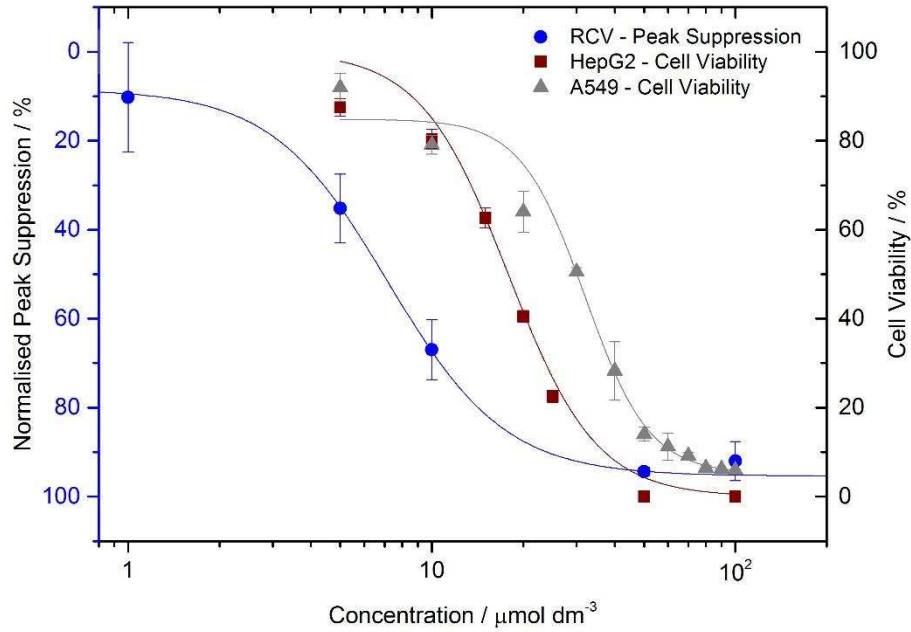


**Figure 8: Normalised percentage suppression of first capacitance-current peak observed on the forward scan of RCV measurements compared against cell viability studies of HepG2 and A549 cells after interaction with chlorpromazine**

A logistic function sigmoidal fit was used for both data sets in Figure 7 and Figure 8, as defined by Equation (1), a fitting typically used for dose response analysis, fitted with the Levenberg Marquardt algorithm [52]:

$$h = h_{\infty} + \frac{(h_o - h_{\infty})}{1 + \left(\frac{c}{EC_{50}}\right)^n} \quad (1)$$

where  $h$  is the peak suppression (%),  $h_{\infty}$  is the peak suppression at the highest concentration (%),  $h_o$  is the initial peak suppression at the lowest concentration (%),  $c$  is the concentration of the biomembrane-active sample ( $\mu\text{mol dm}^{-3}$ ),  $EC_{50}$  is the concentration resulting in a response half way between  $h_o$  and  $h_{\infty}$  ( $\mu\text{mol dm}^{-3}$ ) and  $n$  is a factor that determines the gradient of the curve. All parameters determined from the sigmoidal fit for the dose response curves in Figure 8 are compared in the Supplementary Material. The  $EC_{50}$  measured for the RCV platform using this fit was  $7.2 \mu\text{mol dm}^{-3}$ , whilst the HepG2 and A549 cell lines gave  $EC_{50}$  values of  $17 \mu\text{mol dm}^{-3}$  and  $32 \mu\text{mol dm}^{-3}$  respectively. Broeders et al. [53] also completed cytotoxicity studies of chlorpromazine interaction with human intestinal, human liver and murine fibroblast cell lines and

similarly reported EC<sub>50</sub> values in the range of 7 to 70  $\mu\text{mol dm}^{-3}$ , dependent on the cell line. The phospholipid monolayer sensing technique represents a simplified mimic of a much more complex biological cell structure, therefore some differences between results could be expected. However, exceptional agreement between RCV measurements and cytotoxicity assays was observed. The automated RCV platform, however, achieved the same results in approximately 5 min, compared to 24 h required for the cytotoxicity assay measurements, demonstrating its suitability for robust high-throughput screening.

### 4.3. AuNM

To confirm the new validated screening platform was also effective for its intended purpose of rapid screening of nanomaterials, AuNM was screened. The RCV scans after the interaction of AuNM (red line) with a DOPC monolayer (black line) are shown in Figure 9. All RCV scans are included in the Supplementary Material. An interaction of AuNM with the DOPC monolayer was observed at concentrations above 10  $\mu\text{mol dm}^{-3}$  of Au in the dispersion. No significant interactions were observed at concentrations lower than this. Suppression of the peaks above 10  $\mu\text{mol dm}^{-3}$  was likely caused by AuNM adsorbing to the DOPC monolayer, suppressing the peaks and potentially influencing the fluidity of the phospholipid layer. Vakurov et al. [10] observed similar suppressed RCV peaks after the interaction of silica nanoparticles with a DOPC monolayer, and observed adsorption of the nanoparticles to the DOPC monolayer using SEM. Due to the wide range of properties that nanomaterials can possess, and their subsequent effect on cytotoxicity, direct comparison between the monolayer interactions observed in this study with literature studies cannot be completed easily. For example, it has been shown for both AuNM [51] and zinc oxide nanomaterial [5] that differences of particle size or particle coating can significantly influence the severity of membrane interaction. However, the strong agreement between RCV measurements and *in vitro* cytotoxicity assays observed for chlorpromazine in Figure 8, and a previous study comparing the interaction of silica nanoparticles with the monolayer-on-chip technique and unilamellar vesicles [21], gives credibility to the biological relevance of the electrochemical results representing membrane interactions observed in Figure 9.

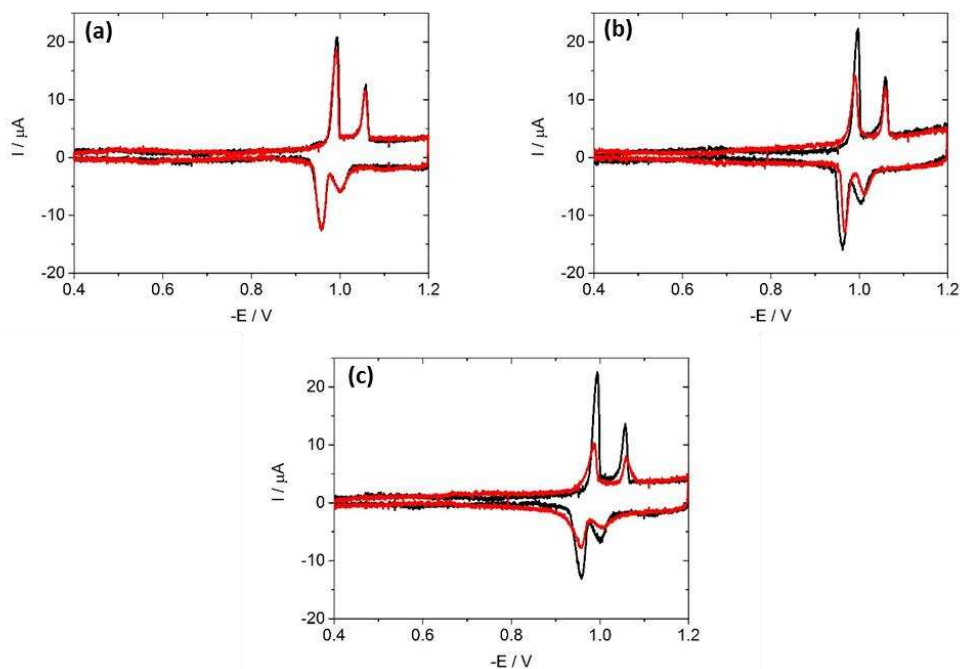


**Figure 9: RCV scans recorded at  $40 \text{ Vs}^{-1}$  of an Hg-supported DOPC monolayer (black line) and interaction with AuNM (red line) with a Au concentration of (a)  $0.001 \mu\text{mol dm}^{-3}$ , (b)  $50 \mu\text{mol dm}^{-3}$  and (c)  $100 \mu\text{mol dm}^{-3}$  in PBS at pH 7.4 (all RCV scans in Supplementary Material)**

The percentage peak suppression of the first capacitance-current peak on the forward scan after interaction of AuNM with the DOPC monolayer is shown in Figure 10. Average peak heights for each AuNM sample screened (six results for each concentration) are compared against the same baseline DOPC peak height ( $19.5 \mu\text{A} \pm 1.4 \mu\text{A}$ ) used for the chlorpromazine analysis of peak suppression, shown in Figure 7. Results from the automated platform were also compared with results of AuNM interaction using the older generation, manual system to demonstrate equivalence between the two platforms. The same average DOPC peak baseline ( $20.9 \mu\text{A} \pm 1.5 \mu\text{A}$ ) for chlorpromazine interactions, in Figure 7, on the manual system was used. The same concentrations of AuNM were screened using the manual system, with the average of three measurements reported in Figure 10. Error bars in Figure 10 for both sets of data represent the standard deviation of the peak suppression measurements. Similar results were obtained for differences between the peak suppressions measured on the automated platform and the manual system, with the average difference between results measured on both platforms equal to 8% peak suppression.

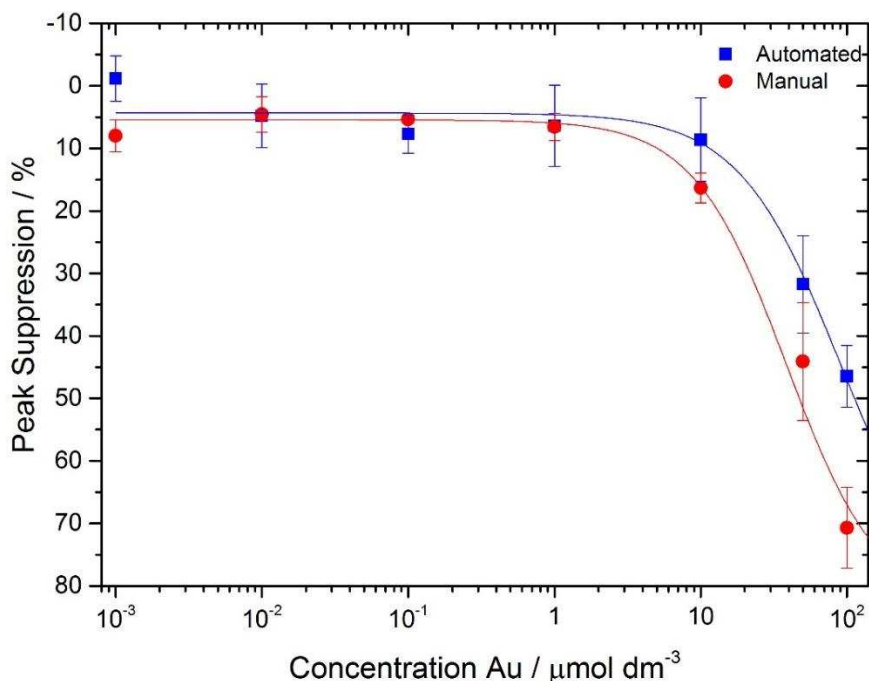


**Figure 10: Percentage suppression of first capacitance-current peak observed on the forward scan of RCV measurements, at a potential of approximately  $-0.96$  V, after interaction of AuNM at different concentrations with an Hg-supported DOPC monolayer electrode in PBS at pH 7.4, showing equivalence between the new automated platform and the manual predecessor biomembrane sensing system**

A sigmoidal fit was used for both data sets in Figure 7, as defined by Equation (1). Concentrations above  $100 \mu\text{mol dm}^{-3}$  could not be screened due to the maximum stock concentration of the AuNM, therefore a value for  $h_{\infty}$  was approximated of  $82.5\% \pm 7.5\%$  to enable a logistic fit to be determined. This was estimated to be the typical maximum peak suppression possible, determined from chlorpromazine results in Figure 7, and RCV responses reported in literature using the same technique [7, 10, 28, 29]. A similar trend was observed between results obtained on the manual system and results obtained on the automated platform. However, the concentrations of AuNM for  $EC_{50}$  were approximately double on the automated platform ( $30 \mu\text{mol dm}^{-3}$ ) compared to the manual system ( $14 \mu\text{mol dm}^{-3}$ ), potentially as a result of minor differences in flow cell design influencing the transport of AuNM to the sensing electrode.

#### 4.4. Viability of Platform for High-Throughput Nanomaterial Screening

This study has presented a viable solution to rapid, high-throughput *in vitro* solutions for sensing nanomaterial-biomembrane interactions. Some of the main challenges required for nanomaterial screening, such as the requirements for high-throughput and

appropriate flow channel designs to allow the required transport of nanomaterials to sensing areas, discussed in Section 1, have been addressed in the new platform design, improving the potential for wider usage of the technique for screening nanomaterials. Despite being a phospholipid monolayer system, and therefore being a simplified mimic of a complex cell membrane structure, a strong correlation was observed for chlorpromazine screening on the automated RCV platform and *in vitro* cell viability studies in HepG2 and A549 cells. However, results on the automated screening platform were obtained in approximately 5 to 6 min per assay, whereas cell viability cytotoxicity results were obtained after 24 h, demonstrating the advantage of using the electrochemical platform for rapid screening. Some mechanistic understanding of the interaction was also gained, with RCV peak suppression likely to be caused by adsorption of the AuNM to the DOPC monolayer.

The platform is ideally suited for investigations of membrane interaction in a range of experimental conditions. Different cell membrane compositions, for example, can be analysed through the use of multiple phospholipids, to create a mixed phospholipid membrane monolayer supported on Hg [35], or through the integration of cholesterol into the supported monolayer [34], widening the potential scope of nanomaterial-biomembrane interaction investigations. Limitations of some cytotoxicity assays, such as the possibility of nanomaterial transformations in the assay, as discussed in Section 1, can also be avoided due to the rapid screening time, enabling a precisely controlled environment for screening nanomaterials.

This work has also demonstrated important improvements to the screening technique, significantly increasing its viability as a high-throughput *in vitro* solution for nanomaterial screening. Throughput was significantly increased, compared to the predecessor system, with screening time reduced from approximately 10 min per assay to 5 – 6 min per assay on the new automated platform. Consumption of PBS was also significantly decreased by at least 50%. Stable DOPC monolayers could be formed on the Pt/Hg electrode, confirmed by consistent and durable peak heights, using only 5 cm<sup>-3</sup> of DOPC, 50% less than consumed on the manual system, as a result of a smaller sensing volume in the new microfluidic flow cell. This also decreased the quantity of waste fluid from the screening. In addition to decreased fluid consumption, the screening process was carried out with much greater ease using the new platform, due to automation of the

system and the development of an easy-to-use user interface. The sensitivity of the electrochemically-measured results to flow rates and consumption of DOPC and PBS could also be investigated more thoroughly as a result of automation. Potential also exists to increase throughput and usability further, by automating data processing to quantify biomembrane activity in real-time and increasing the number of sensing modules integrated on to the platform.

## 5. Conclusion

An automated electrochemical biomembrane screening platform has been developed for the purpose of rapid, high-throughput screening of nanomaterial-biomembrane interactions. The design of the platform has been discussed, with chlorpromazine and AuNM assessed using the screening platform to demonstrate the performance of the system and its viability as a high-throughput sensor for screening nanomaterials. The following conclusions were reached:

- A new screening platform was developed to enhance an existing, well-established technique for sensing biomembrane activity with significantly decreased operator skill level requirements, by automating key aspects of the screening process and integrating automated syringe pumps into the platform design.
- An easy-to-use user interface was developed to control the screening platform and display electrochemical results, simplifying the screening process.
- Chlorpromazine and AuNM were screened using the new platform, with both showing interactions with the DOPC membrane at concentrations of greater than  $1 \mu\text{mol dm}^{-3}$ .
- A strong correlation was observed between RCV-measured biomembrane interaction after the interaction of chlorpromazine with the DOPC monolayer and routine *in vitro* cytotoxicity assays.
- Decreased fluid consumption during screening was achieved by decreasing the volume of tubing required to transport fluids to the flow cell, by designing a new microfluidic flow cell and automated syringe pumps to store and control the flow of fluids into the flow cell, decreasing buffer and DOPC usage by approximately 50% compared to the predecessor screening system.

- Screening time was reduced to <6 min per assay, significantly improving throughout of the technique.

## Supplementary Material

See Supplementary Material for further detail on the CFD turbulence model used, the User Interface developed for the screening platform and for RCV scans of AuNM and chlorpromazine at all concentrations screened using the automated platform.

## Acknowledgments

This work was completed as part of the HISENTS programme which has received funding from the European Union's Horizon 2020 research and innovation programme under grant agreement No. 685817.

## References

1. Damoiseaux, R., George, S., Li, M., Pokhrel, S., Ji, Z., France, B., Xia, T., Suarez, E., Rallo, R., and Mädler, L., *No time to lose—high throughput screening to assess nanomaterial safety*. *Nanoscale*, 2011. **3**(4): p. 1345-1360.
2. De, M., Ghosh, P.S., and Rotello, V.M., *Applications of Nanoparticles in Biology*. *Advanced Materials*, 2008. **20**(22): p. 4225-4241.
3. Mortimer, M., Kasemets, K., Heinlaan, M., Kurvet, I., and Kahru, A., *High throughput kinetic Vibrio fischeri bioluminescence inhibition assay for study of toxic effects of nanoparticles*. *Toxicology in vitro*, 2008. **22**(5): p. 1412-1417.
4. Salata, O.V., *Applications of nanoparticles in biology and medicine*. *Journal of Nanobiotechnology*, 2004. **2**(1): p. 3.
5. Vakurov, A., Mokry, G., Drummond-Brydson, R., Wallace, R., Svendsen, C., and Nelson, A., *ZnO nanoparticle interactions with phospholipid monolayers*. *Journal of colloid and interface science*, 2013. **404**: p. 161-168.
6. Liu, W.-T., *Nanoparticles and their biological and environmental applications*. *Journal of Bioscience and Bioengineering*, 2006. **102**(1): p. 1-7.
7. Vakurov, A., Drummond-Brydson, R., Ugwumsinachi, O., and Nelson, A., *Significance of particle size and charge capacity in TiO2 nanoparticle-lipid interactions*. *Journal of colloid and interface science*, 2016. **473**: p. 75-83.
8. Hansjosten, I., Rapp, J., Reiner, L., Vatter, R., Fritsch-Decker, S., Peravali, R., Palosaari, T., Joossens, E., Gerloff, K., Macko, P., Whelan, M., Gilliland, D., Ojea-Jimenez, I., Monopoli, M.P., Rocks, L., Garry, D., Dawson, K., Röttgermann, P.J.F., Murschhauser, A., Rädler, J.O., Tang, S.V.Y., Gooden, P., Belinga-Desaunay, M.-F.A., Khan, A.O., Briffa, S., Guggenheim, E., Papadiamantis, A., Lynch, I., Valsami-Jones, E., Diabaté, S., and Weiss, C., *Microscopy-based high-throughput assays enable multi-parametric analysis to assess adverse effects of nanomaterials in various cell lines*. *Archives of Toxicology*, 2018. **92**(2): p. 633-649.

9. Gliga, A.R., Skoglund, S., Wallinder, I.O., Fadeel, B., and Karlsson, H.L., *Size-dependent cytotoxicity of silver nanoparticles in human lung cells: the role of cellular uptake, agglomeration and Ag release*. *Particle and fibre toxicology*, 2014. **11**(1): p. 11.
10. Vakurov, A., Brydson, R., and Nelson, A., *Electrochemical modeling of the silica nanoparticle–biomembrane interaction*. *Langmuir*, 2011. **28**(2): p. 1246-1255.
11. Lewinski, N., Colvin, V., and Drezek, R., *Cytotoxicity of nanoparticles*. *small*, 2008. **4**(1): p. 26-49.
12. Lopez-Chaves, C., Soto-Alvaredo, J., Montes-Bayon, M., Bettmer, J., Llopis, J., and Sanchez-Gonzalez, C., *Gold nanoparticles: distribution, bioaccumulation and toxicity. In vitro and in vivo studies*. *Nanomedicine: Nanotechnology, Biology and Medicine*, 2018. **14**(1): p. 1-12.
13. Nel, A., Xia, T., Meng, H., Wang, X., Lin, S., Ji, Z., and Zhang, H., *Nanomaterial toxicity testing in the 21st century: use of a predictive toxicological approach and high-throughput screening*. *Accounts of chemical research*, 2012. **46**(3): p. 607-621.
14. George, S., Xia, T., Rallo, R., Zhao, Y., Ji, Z., Lin, S., Wang, X., Zhang, H., France, B., and Schoenfeld, D., *Use of a high-throughput screening approach coupled with in vivo zebrafish embryo screening to develop hazard ranking for engineered nanomaterials*. *ACS nano*, 2011. **5**(3): p. 1805-1817.
15. Astashkina, A., Mann, B., and Grainger, D.W., *A critical evaluation of in vitro cell culture models for high-throughput drug screening and toxicity*. *Pharmacology & therapeutics*, 2012. **134**(1): p. 82-106.
16. Mahto, S.K., Charwat, V., Ertl, P., Rothen-Rutishauser, B., Rhee, S.W., and Sznitman, J., *Microfluidic platforms for advanced risk assessments of nanomaterials*. *Nanotoxicology*, 2015. **9**(3): p. 381-395.
17. Verma, A. and Stellacci, F., *Effect of surface properties on nanoparticle–cell interactions*. *Small*, 2010. **6**(1): p. 12-21.
18. Churchman, A.H., Wallace, R., Milne, S.J., Brown, A.P., Brydson, R., and Beales, P.A., *Serum albumin enhances the membrane activity of ZnO nanoparticles*. *Chemical Communications*, 2013. **49**(39): p. 4172-4174.
19. Leroueil, P.R., Hong, S., Mecke, A., Baker Jr, J.R., Orr, B.G., and Banaszak Holl, M.M., *Nanoparticle interaction with biological membranes: does nanotechnology present a Janus face?* *Accounts of chemical research*, 2007. **40**(5): p. 335-342.
20. Mu, Q., David, C.A., Galceran, J., Rey-Castro, C., Krzemiński, Ł., Wallace, R., Bamiduro, F., Milne, S.J., Hondow, N.S., and Brydson, R., *Systematic investigation of the physicochemical factors that contribute to the toxicity of ZnO nanoparticles*. *Chemical research in toxicology*, 2014. **27**(4): p. 558-567.
21. Zhang, S., Nelson, A., and Beales, P.A., *Freezing or wrapping: the role of particle size in the mechanism of nanoparticle–biomembrane interaction*. *Langmuir*, 2012. **28**(35): p. 12831-12837.
22. Jones, C.F. and Grainger, D.W., *In vitro assessments of nanomaterial toxicity*. *Advanced drug delivery reviews*, 2009. **61**(6): p. 438-456.
23. George, S., Pokhrel, S., Xia, T., Gilbert, B., Ji, Z., Schowalter, M., Rosenauer, A., Damoiseaux, R., Bradley, K.A., and Mädler, L., *Use of a rapid cytotoxicity screening approach to engineer a safer zinc oxide nanoparticle through iron doping*. *ACS nano*, 2009. **4**(1): p. 15-29.
24. Collins, A.R., Annangi, B., Rubio, L., Marcos, R., Dorn, M., Merker, C., Estrela-Lopis, I., Cimpan, M.R., Ibrahim, M., and Cimpan, E., *High throughput toxicity screening and intracellular detection of nanomaterials*. *Wiley Interdisciplinary Reviews: Nanomedicine and Nanobiotechnology*, 2017. **9**(1): p. e1413.

25. Coldrick, Z., Penezić, A., Gašparović, B., Steenson, P., Merrifield, J., and Nelson, A., *High throughput systems for screening biomembrane interactions on fabricated mercury film electrodes*. Journal of applied electrochemistry, 2011. **41**(8): p. 939-949.
26. Coldrick, Z., Steenson, P., Millner, P., Davies, M., and Nelson, A., *Phospholipid monolayer coated microfabricated electrodes to model the interaction of molecules with biomembranes*. Electrochimica Acta, 2009. **54**(22): p. 4954-4962.
27. Miller, I., Rishpon, J., and Tenenbaum, A., *Electrochemical determination of structure and interactions in spread lipid monolayers*. Bioelectrochemistry and Bioenergetics, 1976. **3**(3-4): p. 528-542.
28. Nelson, A., *Penetration of mercury-adsorbed phospholipid monolayers by polynuclear aromatic hydrocarbons*. Analytica Chimica Acta, 1987. **194**: p. 139-149.
29. Nelson, A., Auffret, N., and Borlakoglu, J., *Interaction of hydrophobic organic compounds with mercury adsorbed dioleoylphosphatidylcholine monolayers*. Biochimica et Biophysica Acta (BBA) - Biomembranes, 1990. **1021**(2): p. 205-216.
30. Nelson, A., Auffret, N., and Readman, J., *Initial applications of phospholipid-coated mercury electrodes to the determination of polynuclear aromatic hydrocarbons and other organic micropollutants in aqueous systems*. Analytica Chimica Acta, 1988. **207**: p. 47-57.
31. Nelson, A. and Benton, A., *Phospholipid monolayers at the mercury/water interface*. Journal of electroanalytical chemistry and interfacial electrochemistry, 1986. **202**(1-2): p. 253-270.
32. Rashid, A., Vakurov, A., Mohamadi, S., Sanver, D., and Nelson, A., *Substituents modulate biphenyl penetration into lipid membranes*. Biochimica et Biophysica Acta (BBA)-Biomembranes, 2017. **1859**(5): p. 712-721.
33. Rashid, A., Vakurov, A., and Nelson, A., *Role of electrolyte in the occurrence of the voltage induced phase transitions in a dioleoyl phosphatidylcholine monolayer on Hg*. Electrochimica Acta, 2015. **155**: p. 458-465.
34. Nelson, A. and Auffret, N., *Phospholipid monolayers of di-oleoyl lecithin at the mercury/water interface*. Journal of electroanalytical chemistry and interfacial electrochemistry, 1988. **244**(1-2): p. 99-113.
35. Neville, F., Gidalevitz, D., Kale, G., and Nelson, A., *Electrochemical screening of anti-microbial peptide LL-37 interaction with phospholipids*. Bioelectrochemistry, 2007. **70**(2): p. 205-213.
36. Ringstad, L., Protopapa, E., Lindholm-Sethson, B., Schmidtchen, A., Nelson, A., and Malmsten, M., *An electrochemical study into the interaction between complement-derived peptides and DOPC mono-and bilayers*. Langmuir, 2008. **24**(1): p. 208-216.
37. Drasler, B., Sayre, P., Steinhäuser, K.G., Petri-Fink, A., and Rothen-Rutishauser, B., *In vitro approaches to assess the hazard of nanomaterials*. NanoImpact, 2017. **8**: p. 99-116.
38. Guadagnini, R., Halamoda Kenzaoui, B., Walker, L., Pojana, G., Magdolenova, Z., Bilanicova, D., Saunders, M., Juillerat-Jeanneret, L., Marcomini, A., and Huk, A., *Toxicity screenings of nanomaterials: challenges due to interference with assay processes and components of classic in vitro tests*. Nanotoxicology, 2015. **9**(sup1): p. 13-24.
39. Kroll, A., Pillukat, M.H., Hahn, D., and Schneckeburger, J., *Current in vitro methods in nanoparticle risk assessment: limitations and challenges*. European journal of Pharmaceutics and Biopharmaceutics, 2009. **72**(2): p. 370-377.
40. Nelson, A., *Electrochemistry of mercury supported phospholipid monolayers and bilayers*. Current Opinion in Colloid & Interface Science, 2010. **15**(6): p. 455-466.

41. Du, G., Fang, Q., and den Toonder, J.M., *Microfluidics for cell-based high throughput screening platforms—A review*. *Analytica chimica acta*, 2016. **903**: p. 36-50.
42. Ríos, Á., Zougagh, M., and Avila, M., *Miniaturization through lab-on-a-chip: Utopia or reality for routine laboratories? A review*. *Analytica chimica acta*, 2012. **740**: p. 1-11.
43. Whitesides, G.M., *The origins and the future of microfluidics*. *Nature*, 2006. **442**(7101): p. 368.
44. Sackmann, E.K., Fulton, A.L., and Beebe, D.J., *The present and future role of microfluidics in biomedical research*. *Nature*, 2014. **507**(7491): p. 181.
45. Nasser, B., Soleimani, N., Rabiee, N., Kalbasi, A., Karimi, M., and Hamblin, M.R., *Point-of-care microfluidic devices for pathogen detection*. *Biosensors and Bioelectronics*, 2018.
46. Zhang, J., Yan, S., Yuan, D., Alici, G., Nguyen, N.-T., Warkiani, M.E., and Li, W., *Fundamentals and applications of inertial microfluidics: a review*. *Lab on a Chip*, 2016. **16**(1): p. 10-34.
47. Valencia, P.M., Farokhzad, O.C., Karnik, R., and Langer, R., *Microfluidic technologies for accelerating the clinical translation of nanoparticles*. *Nature nanotechnology*, 2012. **7**(10): p. 623.
48. Pike, D., Kapur, N., Millner, P., and Stewart, D., *Flow cell design for effective biosensing*. *Sensors*, 2013. **13**(1): p. 58-70.
49. Barker, R., Pickles, B., Kapur, N., Hughes, T., Barmatov, E., and Neville, A., *Flow cell apparatus for quantitative evaluation of carbon steel corrosion during transitions in fluid composition: Application to transition from inhibited hydrochloric acid to sodium chloride brine*. *Corrosion Science*, 2018. **138**: p. 116-129.
50. *COMSOL Multiphysics v5.3a Chemical Reaction Engineering Module User's Guide*. 2017.
51. Rizzo, L.Y., Golombek, S.K., Mertens, M.E., Pan, Y., Laaf, D., Broda, J., Jayapaul, J., Möckel, D., Subr, V., and Hennink, W.E., *In vivo nanotoxicity testing using the zebrafish embryo assay*. *Journal of Materials Chemistry B*, 2013. **1**(32): p. 3918-3925.
52. DeLean, A., Munson, P., and Rodbard, D., *Simultaneous analysis of families of sigmoidal curves: application to bioassay, radioligand assay, and physiological dose-response curves*. *American Journal of Physiology-Endocrinology And Metabolism*, 1978. **235**(2): p. E97.
53. Broeders, J.J., Blaauboer, B.J., and Hermens, J.L., *In vitro biokinetics of chlorpromazine and the influence of different dose metrics on effect concentrations for cytotoxicity in Balb/c 3T3, Caco-2 and HepaRG cell cultures*. *Toxicology in Vitro*, 2013. **27**(3): p. 1057-1064.

# High-throughput electrochemical sensing platform for screening nanomaterial-biomembrane interactions

Joshua Owen<sup>a</sup>, Maksims Kuznecovs<sup>a</sup>, Raeesa Bhamji<sup>b</sup>, Nicola William<sup>b</sup>, Natalia Domenech-Garcia<sup>b</sup>, Michelle Hesler<sup>c</sup>, Thorsten Knoll<sup>c</sup>, Yvonne Kohl<sup>c</sup>, Andrew Nelson<sup>b</sup> and Nikil Kapur<sup>a</sup>

<sup>a</sup> *Institute of Thermofluids, School of Mechanical Engineering, University of Leeds, Leeds, LS2 9JT, United Kingdom*

<sup>b</sup> *School of Chemistry, University of Leeds, Leeds, LS2 9JT, United Kingdom*

<sup>c</sup> *Fraunhofer Institute for Biomedical Engineering IBMT, Joseph-von-Fraunhofer-Weg 1, Sulzbach, Germany*

## SUPPLEMENTARY MATERIAL

### Numerical Study of Flow Cell

To confirm that the flow cell design was appropriate for transporting species to the sensing electrode, CFD simulations of fluid flow and dilute species transport through the flow cell were completed. Chlorpromazine, a pharmaceutical compound (screened in the experimental study) was modelled as a dilute species to confirm transport to the sensing electrode, whilst flow through the flow cell was laminar. COMSOL Multiphysics 5.3a [1] was used to solve a finite element discretisation of the Navier-Stokes equations for fluid flow to simulate laminar flow through the flow cell. Similar studies of flow behaviour through flow cells have been completed to confirm that no undesirable flow conditions, (such as flow recirculation as flow channel thickness expands) influence transport to sensing areas within the flow cell [2, 3]. For an incompressible, steady-state, isoviscous flow with no gravity effects, the continuity and momentum equations are defined as [4]:

$$\nabla \cdot \mathbf{u} = 0 \quad (2)$$

$$\rho(\mathbf{u} \cdot \nabla)\mathbf{u} = -\nabla p + \mu \nabla^2 \mathbf{u} \quad (3)$$

where  $\mathbf{u}$  is the flow velocity field (m/s),  $p$  is the pressure (Pa) and  $\mu$  is the dynamic viscosity (Pa·s).

To simulate the time-dependent transport of a dilute species through an incompressible fluid, the advection-diffusion transport equation was solved:

$$\frac{\partial c}{\partial t} = D\nabla^2 c - \mathbf{u} \cdot \nabla c \quad (4)$$

where  $D$  is the diffusion coefficient of the dilute species.

A three-dimensional model of the flow cell geometry was created and meshed using 103,354 tetrahedral elements, as shown in the cross section of the flow cell in Figure 11, refined through a mesh sensitivity study by increasing the number of elements in the mesh until the minimum number of elements required to achieve a robust solution was determined.

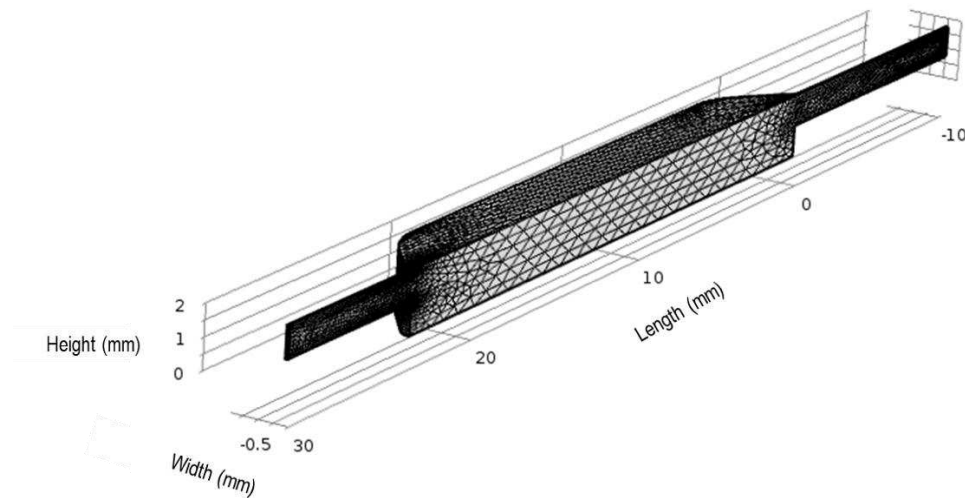


**Figure 11: Cross-section of the 3D model of the flow cell geometry and mesh used to discretise the geometry, consisting of 103,354 tetrahedral elements**

The fluid flow model was solved first, prior to simulating the transport of chlorpromazine through the flow cell. Appropriate boundary conditions were applied to solve the fluid flow and transport equations:

- A pressure boundary condition of 0 Pa was specified at the outlet of the flow cell.
- No-slip conditions applied at the wall (all boundaries in the geometry, excluding the inlet and outlet)
- A symmetry boundary condition was applied to reduce computational effort, on the cross section surface shown in Figure 11
- The fluid was assumed to be water with a density of 998 kg/m<sup>3</sup> and dynamic viscosity of 1 x 10<sup>-3</sup> Pa·s

- The volumetric fluid flow rate into the flow cell was equal to 4.0 cm<sup>3</sup> min<sup>-1</sup>, equivalent to the flow rate used in experimental conditions
- An inflow concentration of 1 mol m<sup>-3</sup> of the dilute species was specified at the inlet of the flow cell, with the initial concentration throughout the geometry set to equal 0 mol m<sup>-3</sup>. A zero flux boundary condition was applied at the walls.
- The dilute species was assumed to be chlorpromazine with a diffusion coefficient estimated to be 2.3 x 10<sup>-9</sup> m<sup>2</sup>/s, determined using the Wilke-Chang equation [5], Equation (5):

$$D = 7.4 \times 10^{-8} \frac{(xM)^{0.5}T}{\mu V^{0.6}} \quad (5)$$

where  $D$  is the diffusion coefficient of a solute (chlorpromazine) in a solvent (water),  $x$  is the association parameter for water (taken as 2.6),  $M$  is the molecular weight of chlorpromazine (355.33 g mol<sup>-1</sup>),  $T$  is the temperature (293 K),  $\mu$  is the dynamic viscosity of water (1 cP) and  $V$  is the molar volume at normal boiling point, reported to be  $\approx 270$  cm<sup>3</sup> mol<sup>-1</sup> for chlorpromazine [6]. The transport of chlorpromazine through the flow cell is shown in the main manuscript represented by the concentration along the bottom surface, to demonstrate the transport of the species to the electrode.

## User Interface

The graphical user interface used to control the automated platform is shown in Figure 12.

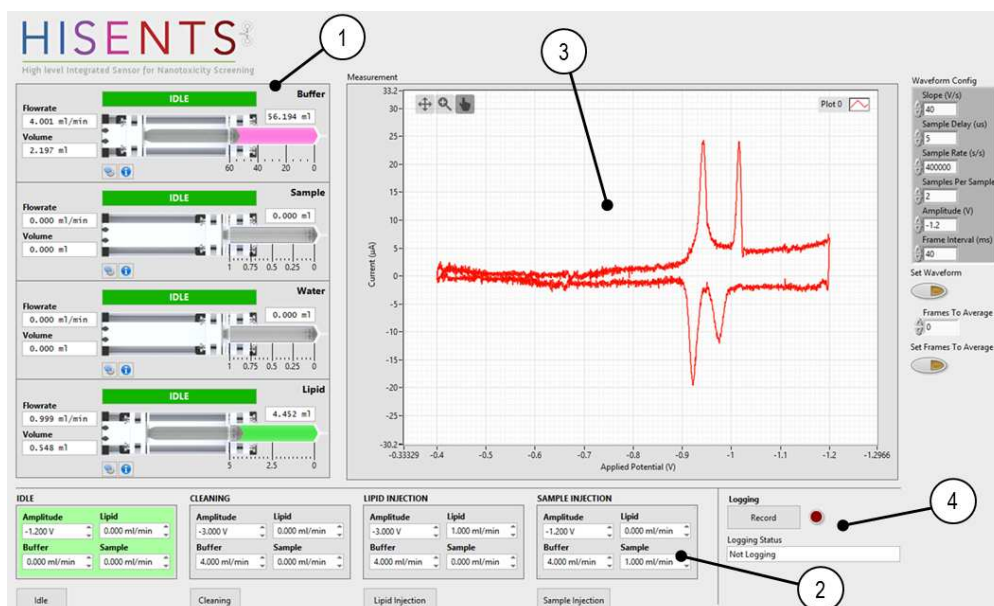


**Figure 12: User control interface consisting of (1) pump configurations, (2) operator controls, (3) real-time RCV response and (4) data export controls**

## Chlorpromazine

The chlorpromazine compound molecular structure screened with the automated and manual platforms is shown in Figure 13.

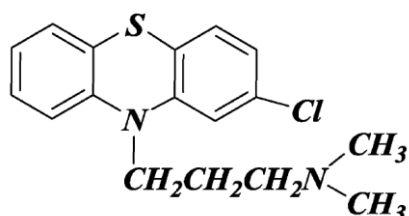


**Figure 13: Chlorpromazine compound molecular structure**

## Chlorpromazine RCV Scans

The RCV scans for each concentration of chlorpromazine screened using the automated biomembrane screening platform after interaction with a DOPC membrane in Figure 6.

The individual fitting parameters determined for the logistic fit are shown in Table 1 for the dose response curve based on normalised peak suppression and cell viability studies for chlorpromazine.

**Table 1: Comparison of the logistic sigmoidal fitting parameters defined by Equation (1) in the main manuscript obtained from automated RCV platform dose**

response curves after interaction of chlorpromazine with the DOPC monolayer compared against HepG2 and A549 cell viability studies

Method	$h_o$ (%)	$h_\infty$ (%)	n	EC <sub>20</sub> ( $\mu\text{mol dm}^{-3}$ )	EC <sub>50</sub> ( $\mu\text{mol dm}^{-3}$ )	EC <sub>80</sub> ( $\mu\text{mol dm}^{-3}$ )
RCV	8.4	95	2.3	3.9	7.2	13
HepG2	100	0	3	11	17	28
A549	84	5.2	4.1	23	32	45

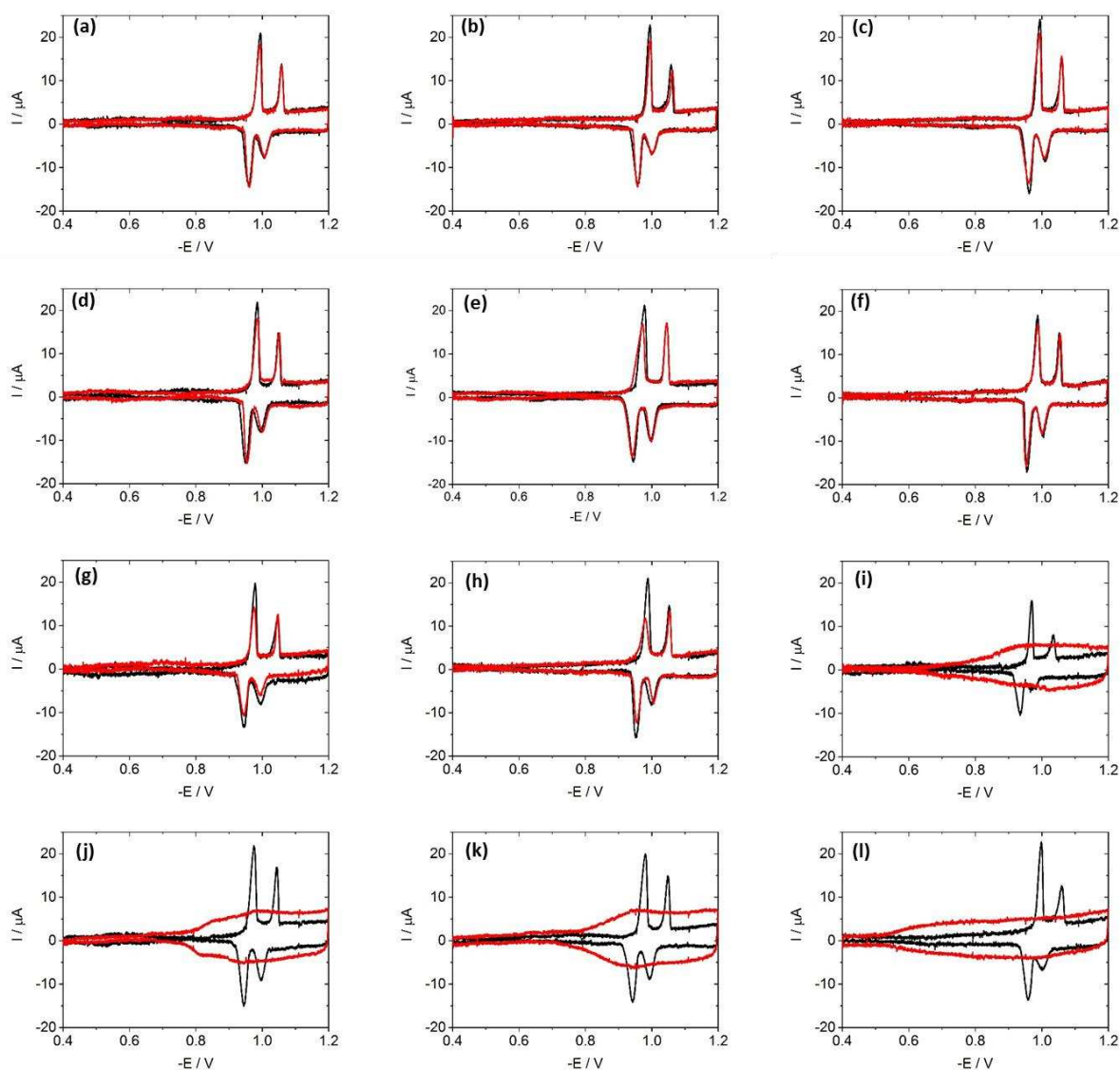
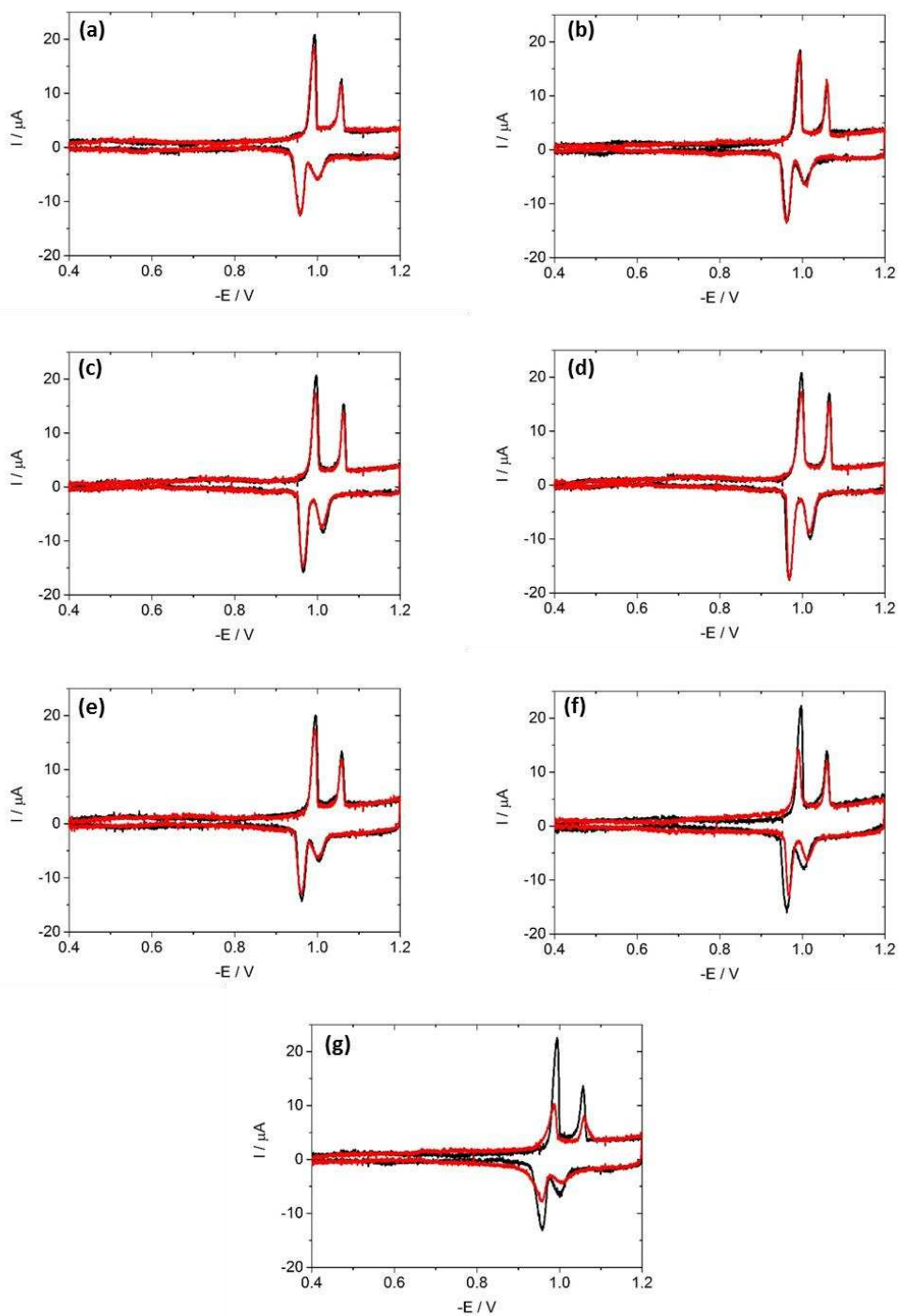


Figure 14: RCV scans, measured using the automated screening platform at a scan rate of  $40 \text{ V s}^{-1}$ , of a DOPC-coated Pt/Hg electrode (black line) and interaction with chlorpromazine (red line) in concentrations of (a)  $10^{-5} \mu\text{mol dm}^{-3}$ , (b)  $10^{-4} \mu\text{mol dm}^{-3}$ , (c)  $10^{-3} \mu\text{mol dm}^{-3}$ , (d)  $10^{-2} \mu\text{mol dm}^{-3}$ , (e)  $10^{-1} \mu\text{mol dm}^{-3}$ , (f)  $1 \mu\text{mol dm}^{-3}$ , (g)  $5 \mu\text{mol dm}^{-3}$ ,

(h)  $10 \mu\text{mol dm}^{-3}$ , (i)  $50 \mu\text{mol dm}^{-3}$ , (j)  $10^2 \mu\text{mol dm}^{-3}$ , (k)  $10^3 \mu\text{mol dm}^{-3}$  and (l)  $10^4 \mu\text{mol dm}^{-3}$  in PBS at pH 7.4

## 6. AuNM RCV Scans

The RCV scans for each concentration of AuNM screened using the automated biomembrane screening platform after interaction with a DOPC membrane in Figure 9.



**Figure 15: RCV scans recorded at  $40 \text{ Vs}^{-1}$  of a DOPC-coated Pt/Hg electrode (black solid line) and interaction with AuNM (red dashed line) with a Au concentration of (a)  $0.001 \mu\text{mol dm}^{-3}$ , (b)  $0.01 \mu\text{mol dm}^{-3}$ , (c)  $0.1 \mu\text{mol dm}^{-3}$ , (d)  $1 \mu\text{mol dm}^{-3}$ , (e)  $10 \mu\text{mol dm}^{-3}$ , (f)  $50 \mu\text{mol dm}^{-3}$  and (g)  $100 \mu\text{mol dm}^{-3}$  in PBS at pH 7.4**

The individual fitting parameters determined for the logistic fit are shown in Table 2 for the dose response curves based on peak suppression results for AuNM for both the manual system and automated platform.

**Table 2: Comparison of the logistic sigmoidal fitting parameters defined by Equation (1) in the main manuscript obtained from the manual and automated platform dose response curves after interaction of chlorpromazine with the DOPC monolayer**

Platform	$h_0$ (%)	$h_\infty$ (%)	n	EC <sub>20</sub> ( $\mu\text{mol dm}^{-3}$ )	EC <sub>50</sub> ( $\mu\text{mol dm}^{-3}$ )
<b>Automated</b>	4.3 ± 1.7	84 ± 5.5	1.3 ± 0.4	30 ± 11	89 ± 18
<b>Manual</b>	5.4 ± 0.3	84 ± 3.7	1.4 ± 0.2	14 ± 1.7	39 ± 6.2

## References

1. COMSOL Multiphysics v5.3a Chemical Reaction Engineering Module User's Guide. 2017.
2. Barker, R., Pickles, B., Kapur, N., Hughes, T., Barmatov, E., and Neville, A., *Flow cell apparatus for quantitative evaluation of carbon steel corrosion during transitions in fluid composition: Application to transition from inhibited hydrochloric acid to sodium chloride brine*. Corrosion Science, 2018. **138**: p. 116-129.
3. Pike, D., Kapur, N., Millner, P., and Stewart, D., *Flow cell design for effective biosensing*. Sensors, 2013. **13**(1): p. 58-70.
4. Versteeg, H.K. and Malalasekera, W., *An introduction to computational fluid dynamics: the finite volume method*. 2007, Harlow: Pearson Education.
5. Wilke, C. and Chang, P., *Correlation of diffusion coefficients in dilute solutions*. AIChE Journal, 1955. **1**(2): p. 264-270.
6. Attwood, D., Mosquera, V., Rey, C., and Garcia, M., *Temperature dependence of molar volume and adiabatic compressibility of aqueous solutions of an amphiphilic phenothiazine drug*. Journal of colloid and interface science, 1991. **147**(2): p. 316-320.